UNIVERSITY OF LEEDS

This is a repository copy of *Engineering design of artificial vascular junctions for 3D printing.*.

White Rose Research Online URL for this paper:
http://eprints.whiterose.ac.uk/101597/

Version: Accepted Version

Article:

White Rose
university consortium
Universities of Leeds, Sheffield & York

eprints@whiterose.ac.uk
https://eprints.whiterose.ac.uk/

Engineering Design of Artificial Vascular Junctions for 3D Printing

Xiaoxiao Han[a,b]*, Richard Bibb[b], Russell Harris[c]

[a] Wolfson school of Mechanical, Electrical and Manufacturing Engineering, Loughborough University, Loughborough. Leicestershire, LE11 3TU, UK

[b] Loughborough Design School, Loughborough University, Loughborough. Leicestershire, LE11 3TU, UK

[c] School of Mechanical Engineering, University of Leeds, Leeds, LS2 9JT, UK.

*corresponding author, Email: x.han2@lboro.ac.uk, Tel: +44 (0)1509 227567

12 **Abstract**

13 Vascular vessels, including arteries, veins and capillaries, are being printed using additive

14 manufacturing technologies, also known as 3D Printing. This paper demonstrates that it is important

15 to follow the vascular design by nature as close as possible when 3D printing artificial vascular

16 branches. In previous work, the authors developed an algorithm of computational geometry for

17 constructing smooth junctions for 3D printing. In this work, computational fluid dynamics (CFD) is

18 used to compare the wall shear stress and blood velocity field for the junctions of different designs.

19 The CFD model can reproduce the expected wall shear stress at locations remote from the junction.

20 For large vessels such as veins, it is shown that ensuring the smoothness of the junction and using

21 smaller joining angles as observed in nature is very important to avoid high wall shear stress and

22 recirculation. The issue is however less significant for capillaries. Large joining angles make no

23 difference to the hemodynamic behavior, which is also consistent with the fact that most capillary

24 junctions have large joining angles. The combination of the CFD analysis and the junction

25 construction method form a complete design method for artificial vascular vessels that can be 3D

26 printed using additive manufacturing technologies.

29

30   **Nomenclature**

31

32   C_{max} Non-dimensionalised maximum curvature of a bifurcation junction

33      $\overline{V}$ Non-dimensionalised branch Volume

34   p_{outlet} Outlet pressure

35   v_{inlet} Inlet velocity

36   x, y, z Cartesian coordinates

37   u_d Control parameters

1. Introduction
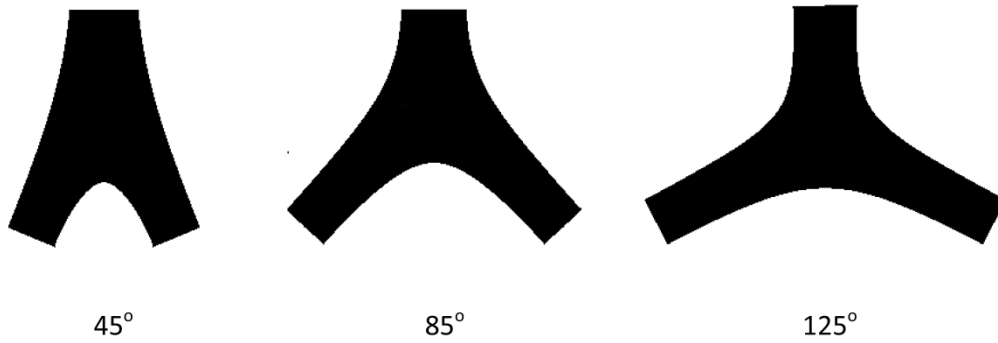
3D Printing has made it possible for the first time to manufacture artificial blood vessels and their networks of any sophisticated geometry and connections. The printed vascular vessels can be used as grafts to treat inadequate blood flow or alongside organ transplantation (Edelman, 1999). In this case, polymers such as poly-propylene-glycol are printed layer by layer to construct a graft which will remain permanently inside the human body. Printed vascular networks can also be used in tissue engineering for regenerative medicine. In this case, biodegradable polymers such as poly-lactide-acid are printed to fabricate a scaffold for the endothelial cells to regenerate into blood vessels. Tissue engineering using a single graft offers potential advantages over conventional autologous or synthetic grafts (Edelman, 1999; Naito and Rathore, 2011). A major issue in organ tissue engineering is that the artificial organ may not develop adequate vascularisation for long-term survival (R.A.J. and O.C., 2002). An artificial micro-vascular network can provide nutrients and soluble growth factors to cells and tissues as well as acting as a scaffold for culturing endothelial cells for capillaries (Patrick Jr, 2000; Kannan et al., 2005; Kamel et al., 2013). The additive manufacturing technology offers the complete freedom to design the details of a vascular branch. Currently various research groups have successfully 3D printed and tested such vascular vessels (Wu et al., 2011; Miller et al., 2012; Kucukgul et al., 2013; Hoch et al., 2014; Kolesky et al., 2014). However, a general guidance on the design of the vascular branch is missing. There have been many published works studying the blood flow and wall shear stress in vascular networks using computational fluid dynamics (CFD). For example, the effect of branching angles on hemodynamics of bifurcations was investigated in great detail in (Friedman et al., 1983; Rabinovitz et al., 1987; Friedman and Seed, 1993; Edelman, 1999; Liu et al., 2015). It was concluded that the branching angle affects the distribution of the flow field in the branch. The flow will become fully developed downstream. The developed rate is determined by the Reynolds number. Local recirculation may occur inside a branch where the cells and nutrients aggregate. The wall shear stress (WSS) is a key hemodynamic indicator that affects the endothelial cell development (Ravensbergen et al., 1995; Ravensbergen et al., 1997; Kohler et al., 2001; Marshall et al., 2004). WSS outside a normal range between 1Pa to 7Pa (Papaioannou and Stefanadis, 2004) is considered harmful to vessel development and may lead to cardiovascular diseases (Kohler et al.,

4

66   2001; Caro, 2008; Coppola and Caro, 2008). However, the previous CFD studies were not aimed at

67   providing guidance for the design of 3D printed vascular vessels. Issues related to 3D printing have

68   not been studied. In the current practice, vascular networks are 3D printed without little understanding

69   of their hemodynamics. "Artificial vascularised scaffolds for 3D-tissue regeneration (ArtiVasc 3D)" is

70   a large project funded by the European Union's Seventh Framework Programme that aims to generate

71   fully vascularised bioartificial skin. The work described in this paper is part of ArtiVasc 3D. In

72   previous work, the authors developed an algorithm of computational geometry for the construction of

73   vascular branch. The algorithm uses three main geometric parameters to control the branch geometry.

74   They are branch angle, volume and maximum curvature at the apex. Three-dimensional models of

75   vascular vessels are generated which can be translated into STL (Stereolithography) data file for 3D

76   Printing (Gibson et al., 2010).

77   The purpose of this paper is to present general guidance on the design of vascular branches. CFD

78   simulations are performed for artificial branches targeted for veins and micro-vascular vessels

79   respectively. For each type of vascular branch, the effect of branch angle and local curvature on the

80   blood flow behavior and WSS are studied. A laminate CFD model in commercial software, COMSOL,

81   was used. Confidence in the CFD model was achieved by the fact that it reproduced the measured wall

82   shear stresses away from the branch. For the large veins, it is shown that ensuring the smoothness of

83   the junction and keeping a relatively small branch angle, as observed in human body, is very

84   important to avoid high wall shear stress and recirculation. The issue is however less significant for

85   capillaries. The branch angle in capillaries has little effect on the WSS, which can also be explained

86   by the fact that capillaries in nature often have large branch angles. The combination of the CFD

87   analysis and the junction construction algorithm form a complete design method for the vascular

88   vessels.

89   **2. Design of vascular branches and their CFD models**

90   We consider artificial vascular vessels targeted for veins and micro-vascular vessels, respectively.

91   Vascular branches are constructed using the algorithm described in (Han et al., 2015). Figure 1 shows

92   the mid-sections of the smooth branches with three different joining angles of 45°, 85°, and 125°.

45°   85°   125°

93

94   Figure 1. Mid-sections of the smooth branches with joining angles of 45°, 85°, and 125°.

95   The branch is made by joining three circular tubes of two different diameters. For the veins, the

96   diameters are 5mm and 3.87mm, respectively (Ravensbergen et al., 1995; Ravensbergen et al., 1997).

97   The dimensions of the model were based on a morphological study of 85 human vertebra-basilar

98   specimens. The ratio between the total cross-sectional area of the two inlet tubes and the cross-

99   sectional of the outlet tube is equal to 1.2 which is biologically realistic according to (Ravensbergen et

100   al., 1995). For the micro-vascular vessels, the diameters are 0.05mm and 0.0387mm, respectively. The

101   shape of the junction profile shown in Figure 1 is taken as a Bezier curve [1]. Bezier curve uses a

102   parameter u_d to complete the definition of the curve, which is fully explained in [1]. Table 1 provides

103   the values of u_d for cases studied in this work. The different values of u_d lead to different maximum

104   curvatures of the junction, which are also provided in Table 1.

105   Table 1. Value of controlled variables for different cases

Parameters / Cases	Branch angle	$\overline{C}_{max}$	$\overline{V}$	u_d
1	125°	0.44	5.4	0.89
2	85°	1.43	5.4	0.84
3	45°	1.34	5.9	0.4
4	45°	3.02	5.56	0.53
5	45°	5.37	5.4	0.6
6	45°	7.5	5.3	0.63
7	45°	14	5.2	0.674

106

107   The curvature is normalised by the diameter of the larger tube. Five different curvatures are used for

108   the branches with joining angle of 45° to study the effect of different curvatures. As an extreme

109   example of unnatural design, vascular junctions are also constructed using rectangular tubes of two

110   different sizes. Bezier curves are not used to smooth the junction. The dimensions of the rectangular
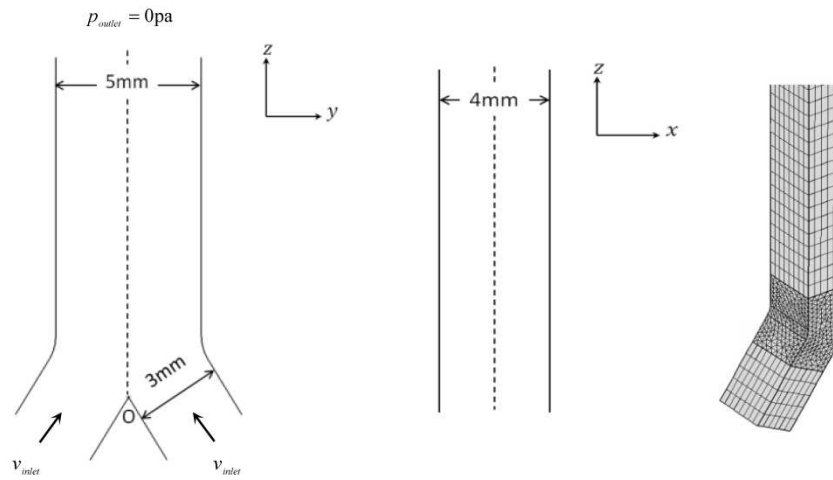
111   tube are provided in figure 2.

112

120   Figure 2. Sharp branching dimensions and boundary conditions.

121   These dimensions are selected to ensure the circular and rectangular tubes have roughly the same

122   cross section area. The junction is connected to two inlet tubes of 70mm and one outlet tube of

123   200mm (Ravensbergen et al., 1995; Ravensbergen et al., 1997).

124   The model makes the following assumptions:

125   •   The flow is laminar, incompressible and Newtonian;

126   •   Only steady state flow is considered;

127   •   The vessel walls are assumed as rigid with no-slip conditions;

128   When steady state and incompressible conditions are assumed, the Navier-Stoke equation can be

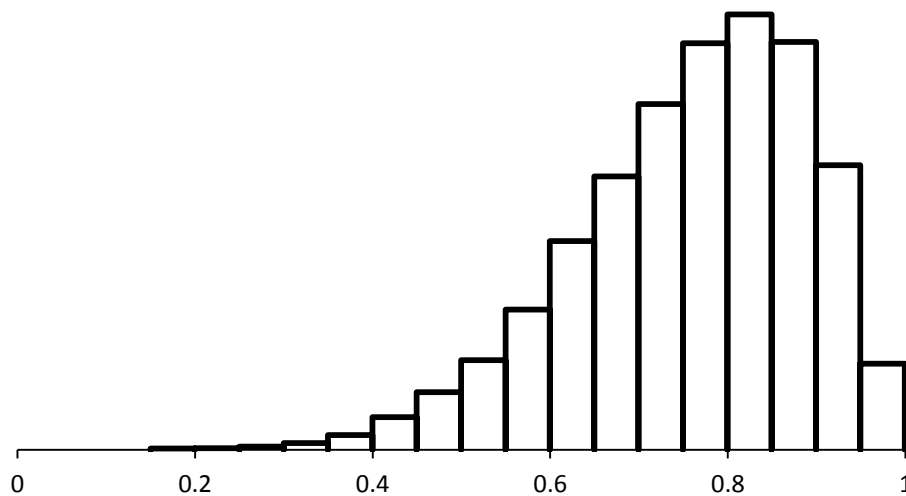129   written in terms of the velocity $\mathbf{u}$ and pressure $_p$:

130 $$-\varepsilon\Delta\mathbf{u}+\mathbf{u}\cdot\nabla\mathbf{u}+\nabla p=\mathbf{f} \quad \text{in } \Omega \tag{1}$$

131
$$\nabla \cdot \mathbf{u} = 0 \quad \text{in } \Omega \tag{2}$$

132   where ε is the viscosity and $\mathbf{f}$ is the body force per unit mass. In this study, ε is set as 0.003Pa.s

133   following (Ravensbergen et al., 1995). As the boundary conditions, the inlet velocity at the two

134   smaller tubes is set as 0.465m/s (Ravensbergen et al., 1997) while the outlet pressure at the larger tube

135   is set as zero (Ravensbergen et al., 1997). Previous studies have shown that the flow behavior in the

136   junction is insensitive to the actual value of the outlet pressure because of the large length of the outlet

137   tube used in the model. The Reynolds number is 600 for veins and 0.06 for micro-vascular vessels

138   both of which are within the normal range of human blood flow (Cliff, 1976). The CFD module of

139   commercial software COMSOL® was used to solve the equations. A series of convergence studies

140   were performed to ensure the finite element meshes are fine enough to produce the correct solutions.

141   Two types of statistical studies were also performed here to ensure the convergence of the solutions

142   for bifurcation angle $63°$.

143

144   Figure 3. Histogram of mesh element quality distribution

145

146   Figure 3 shows a mesh element quality distribution histogram. The x axis in figure 3 is the quality

147   indicator for mesh elements. For a best element, the indicator equals 1 and for other meshes, the

148   indicator is in the range of $(0,1]$. Bad elements have smaller values. In statistics, the median value of

149   this distribution is 0.55; the mean value of this distribution is 0.76 and the mode value is 0.85. All

150   three values are over 0.5 which indicates a good quality of the meshes. Another statistical study is

8

151   convergence study of the solver we applied to solve CFD simulations. The solver applied is called a

152   stationary solver which is used to solve steady-state problems. More precisely, Newton nonlinear

153   method was applied in COMSOL[®]. In this method, the iterative solver iterates until a relative

154   tolerance is fulfilled. The tolerance was set to be 0.0001 in the solver.

155

156   Figure 4. Relative error versus the iteration number of Newton nonlinear solver

157   Figure 4 indicates the relative error versus the iteration number. It can be seen from figure 4 that after

158   8 iterations, the relative error was smaller than the set tolerance (0.0001). In other words, the results

159   were converged. These two statistical studies validated that the computational results are numerically

160   correct with the same boundary conditions and similar meshes.

161   Ravensbergen et al. (Ravensbergen et al., 1995; Ravensbergen et al., 1997) measured the velocity

162   distributions for the junction made of rectangular tubes as described above. Figure 5 shows the

163   comparison between the CFD simulation and their experimental measurement.
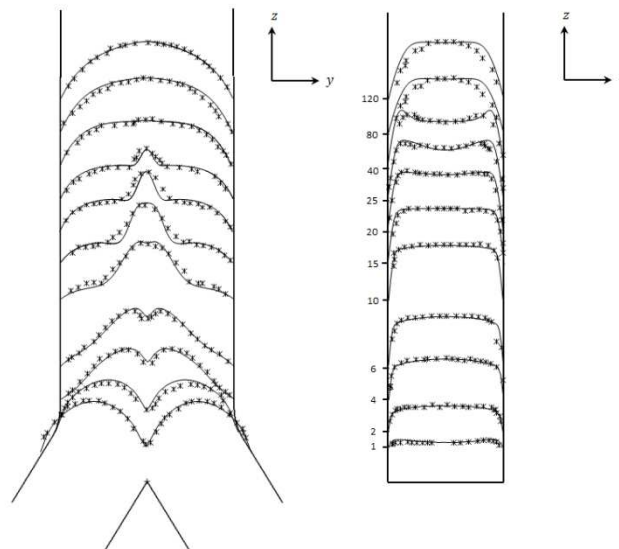
164

165

166

167

168

169

170

171

172

173

174

Figure 5. Simulation results (lines) and experimental data (discrete symbols) (Ravensbergen et al., 1995) comparisons for branching angle $63°$ in (a) yz plane and (b) xz plane.
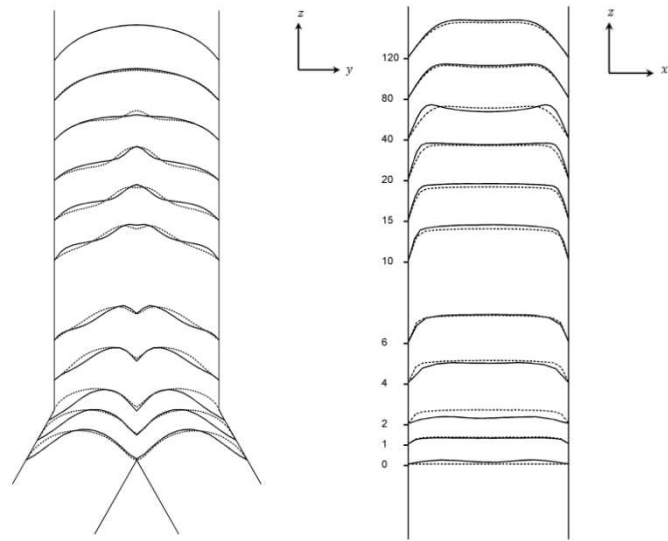
The continuous lines in the figure are simulation results while the discrete symbols are corresponding experimental measurement taken from (Ravensbergen et al., 1995). All the velocities are scaled by the mean axial velocity in the z direction. Figure 5(a) shows the velocity profiles in the $y-z$ central plane while Figure 5(b) shows the velocity profiles in the $x-z$ central plane. The values shown in Figure 5(b) indicate the distances (mm) in the z-direction measured from the branching point. It can be observed from the figure that the numerical and experimental results agree almost perfectly with each other. The maximum error is around 5%. The CFD model can therefore be accepted as accurate enough for the branch design.

3. Hemodynamic analysis for different branch designs

CFD simulations are carried out for branches of different designs outlined at the beginning of section 2. The purpose of the analysis is to compare the different designs in terms of the wall shear stress (WSS) and flow behavior. As explained in the Introduction, WSS is the most important hemodynamic factor when designing a vascular network. Local recirculation should also be minimized to avoid nutrients (for arteries) or waste (for veins) to be trapped in a junction. The CFD results are presented in this section firstly for large vein vessels and then for micro-vascular vessels.
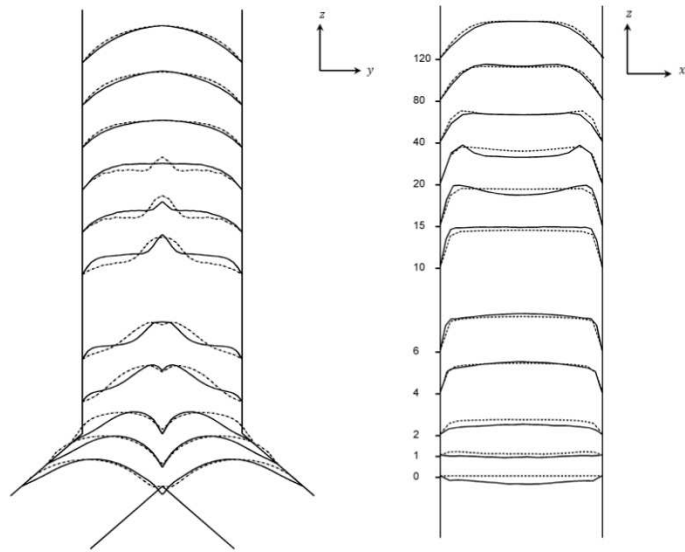
3.1. CFD analysis for large vein branches

CFD simulations were performed for cases 1, 2, and 5. In all cases two flows merge from the daughter vessels into the branch leading to a volume expansion. Using the same branching volume for all the three cases, the effect of branch geometry such as the branching angles can be analyzed. Figure 6 illustrates the simulated velocity profiles for both sharp junctions (interrupted lines) and smoothed junctions (continuous lines) in the xz and yz directions, respectively.
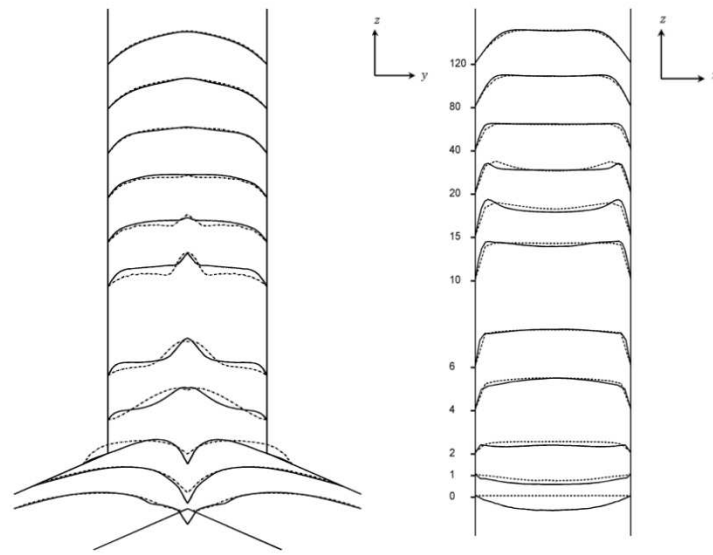
(a) 45°: Case 5

200

(b) 85°: Case 2

201

(c)   125°: Case 1

Figure 6. Comparisons between simulated velocity profiles in sharp branching junction (interrupted lines) and smoothed junctions (continuous lines) for angle (a) $45°$ (b) $85°$ (c) $125°$ in both yz plane and xz planes.

The branching angles of $45°, 85°$ and $125°$ were used in these simulations. The interrupted lines and continuous lines at the bottom of in Figures 6(a-c) in xz and yz directions, compare the velocity profiles at the confluence positions for the sharp junctions and the same positions for the smoothed junctions, respectively. Two humps can be observed in both case 1 and the corresponding sharp junction in the area of influence. In case 1, some negative velocities are observed, the values of which are larger than their sharp counterparts indicating a larger backflow. The two humps begin to merge downstream and start to generate peaks after $z = 6$ mm for both models. However, the peaks in the smoothed branch are narrower compared to that in the sharp branch. The flow becomes uniform further downstream for both smoothed and sharp branches. The flow profile of the smoothed model tends to fully develop quicker than that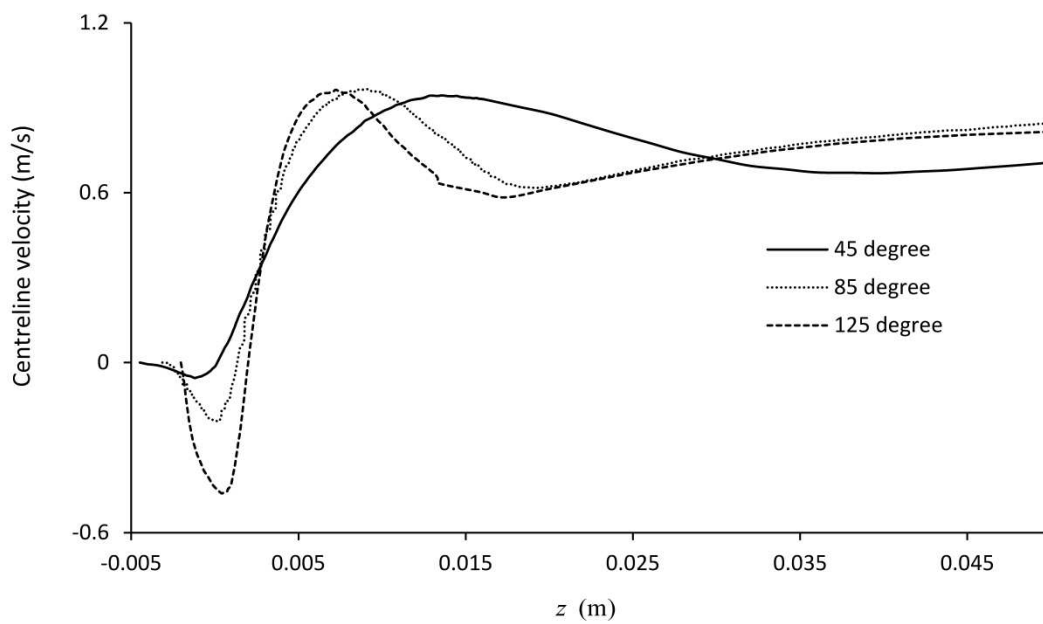 of the sharp one while the peak profile disappears earlier. At the end of the outlet, the two flow profiles are nearly identical. Similar trends are observed in cases 2, 5 and their corresponding sharp counterparts. Three trends can be concluded by observing Figure 6: 1)

12

219　　the magnitude of the negative flow at the branching point is larger for larger branching angle; 2) the

220　　velocity profiles become smooth faster in the smoothed junctions compared with the sharp junctions;

221　　3) the velocity profiles from rounded junctions approach those in the sharp junctions quicker for larger

222　　branching angles. This also indicates that the branching angle has less influence in the smoothed
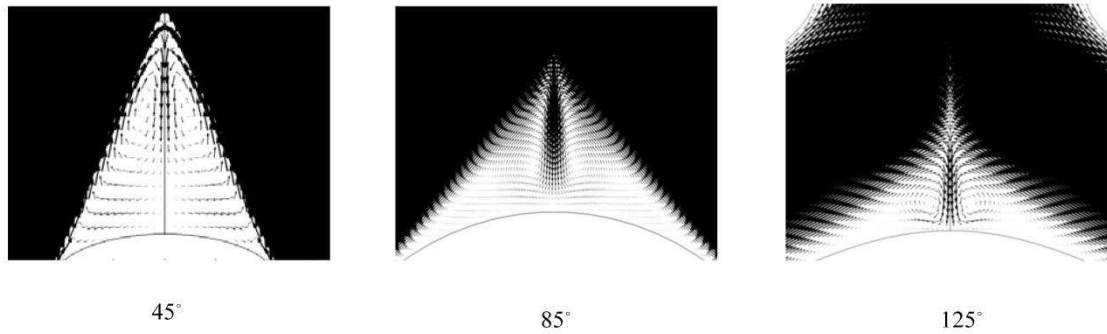
223　　junctions.

224　　　To further demonstrate trend one in a two dimensional manner, two dimensional velocity

225　　distribution around the axial centerline are presented in Figure 7 for branching angles of $45°$, $85°$ and

226　　$125°$.

227

228　　　　Figure 7. Centreline velocities for branching angles $45°$ (case 5), $85°$ (case 2) and $125°$ (case 1).
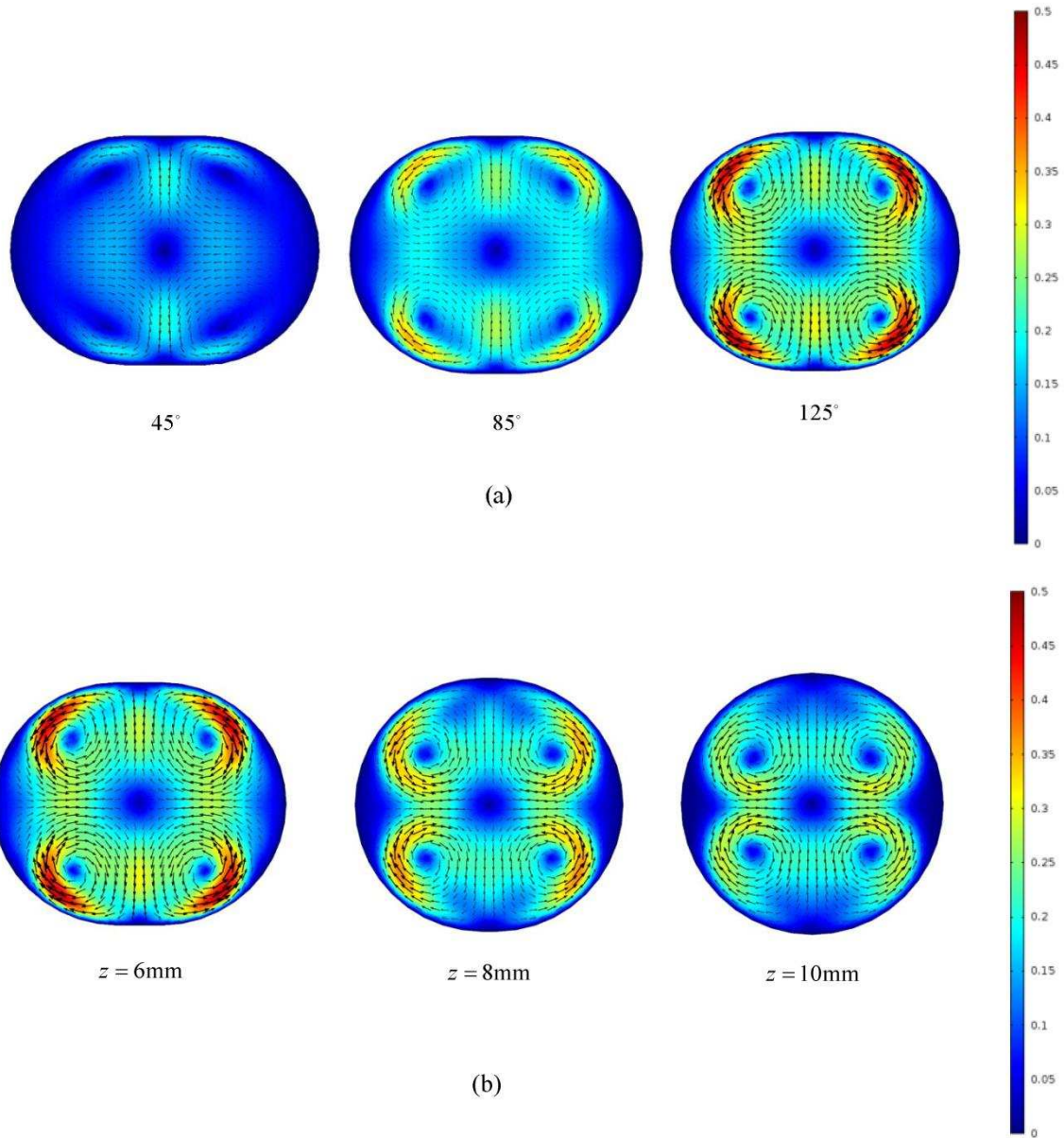
229　　Negative velocities can be observed in the branching areas for all the three smoothed junctions. A

230　　junction with a larger branching angle has a larger value of negative velocity. The larger the branching

231　　angles, the more it increases in the z-direction. At the range of $z = \sim 0.006$ to $0.015 \mathrm{m}$, all the

232　　velocities reach their peak values. The junctions with larger bunching angles reach their peak values

13

233   first. The centerline velocities decrease afterwards and then increase gradually further downstream for

234   all cases. The negative velocity observed in all the cases indicates backflow. In Figure 8, it can be

235   observed that the backflow induces recirculation in the branching area.

45°   85°   125°

236

237   Figure 8. Recirculation area for branching angles $45°$ (case 5), $85°$ (case 2) and $125°$ (case 1).
238

239   Two vortices can be seen in the branching area although its magnitude is small comparing with the

240   surrounding velocity field. A region with low velocity vortices is known as a flow recirculation area.

241   Nutrients for arteries or waste for veins in the blood flow can be trapped in such area. Therefore, it is

242   important to understand how the recirculation area of a rounded junction affects the flow velocity

243   profile and the wall shear stress (WSS) downstream. In figure 8, the ratios of recirculation area over

244   the whole branch are 1) $45°$: 26.4% , 2) $85°$: 24.9% and 3) $125°$: 21.8%. Junction with $45°$ branch

245   angle has the largest recirculation area while junction with $125°$ branch angle has the smallest

246   recirculation area. Although the junction at $125°$ has the largest backflow, its recirculation area has the

247   least influence on the velocity profile downstream. In order to explain this, the secondary velocity

248   distribution for different cases at $z = 6\text{mm}$ is shown in Figure 9 (a) while those for branching angle of

249     $125°$ are shown in Figure 9 (b) at the positions of $z = 6\text{mm}$, $z = 8\text{mm}$ and $z = 10\text{mm}$.
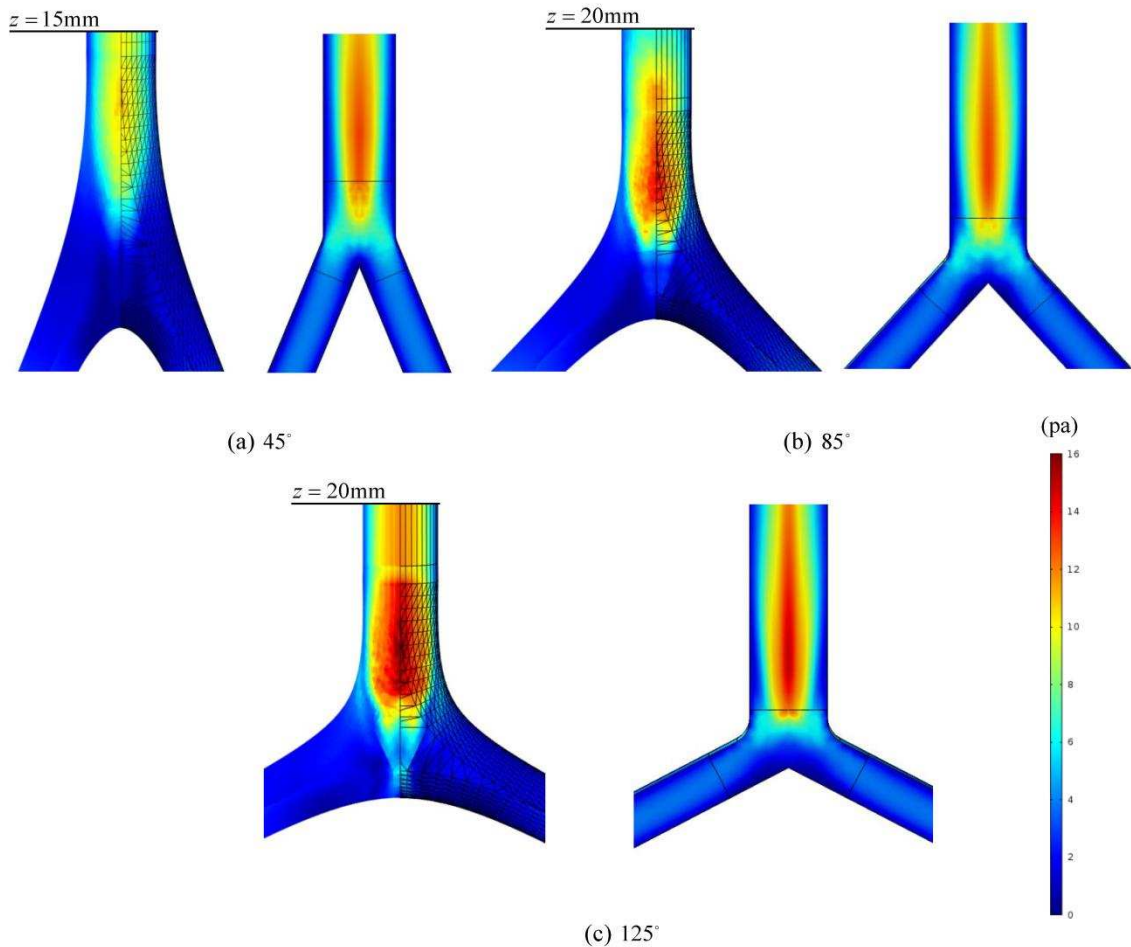
Figure 9. Secondary velocities for (a) branching angles $45°$, $85°$ and $125°$ at $z = 6\text{mm}$ and (b) branching angle $125°$ at $z = 6\text{mm}$, $z = 8\text{mm}$ and $z = 10\text{mm}$

The vectors and magnitudes of the secondary velocity are presented in Figure 9 using colour plots for the three models. Four vortices can be found in each cross section. Figure 9 (a) illustrates a larger magnitude of the secondary velocity in the case of larger branching angle. A strong secondary vortex helps the two flows from the daughter vessels to mix well, which explain why in Figure 7 the flow profiles develop quicker in the cases of larger branching angles. A strong secondary vortex in a

15

260   smoothed branching junction with a large branching angle diminishes the influence of the backflow.

261   This explains that even the backflow at the branching point of a larger angle junction is faster; its

262   influence on the velocity profile downstream is weaker. Hence, the main factor that influences the

263   downstream velocity profile is the size of the recirculation area rather than the strength of the

264   backflow. Figure 9 (b) presents secondary velocities for smoothed junctions with a confluence angle

265   of $125°$ at different downstream positions of $z=6\text{mm}$, $z=8\text{mm}$ and $z=10\text{mm}$. It is obvious that the

266   strength of the vortices decreases as z increases. The vortices disappear once the flow is fully

267   developed.

268   The WSS is one of the most significant hemodynamic factors that relate to blood vessel

269   development and cardiovascular diseases (Kohler et al., 2001; Caro, 2008; Coppola and Caro, 2008).

270   In healthy cerebral arteries, the WSS ranges from 1 Pa to 7 Pa (Papaioannou and Stefanadis, 2004).

271   WSS higher than 7 Pa can damage the endothelial cells during vascular remodeling while WSS lower

272   than 1 Pa can lead to the formation of plaque due to insufficient mechanical stimulation on endothelial

273   cells (Papaioannou and Stefanadis, 2004). WSS distributions for different smoothed cases and their

274   sharp counterparts are shown in Figure 10.

275

Figure 10. Wall shear stress distribution for branching angles (a) $45°$, (b) $85°$ and (c) $125°$ for the smoothed model (left) and sharp model (right).

In the junction, the WSS can be many times higher than that in the straight vessel. WSS in the smoothed junction has a different distribution compared with those in the sharp junctions. High WSS (12 Pa) is found on the sharp junction compared to the rounded one (10 Pa) as shown in Figure 10 (a). The area of low WSS in the smoothed junction is larger than that in the sharp one due to recirculation. Fig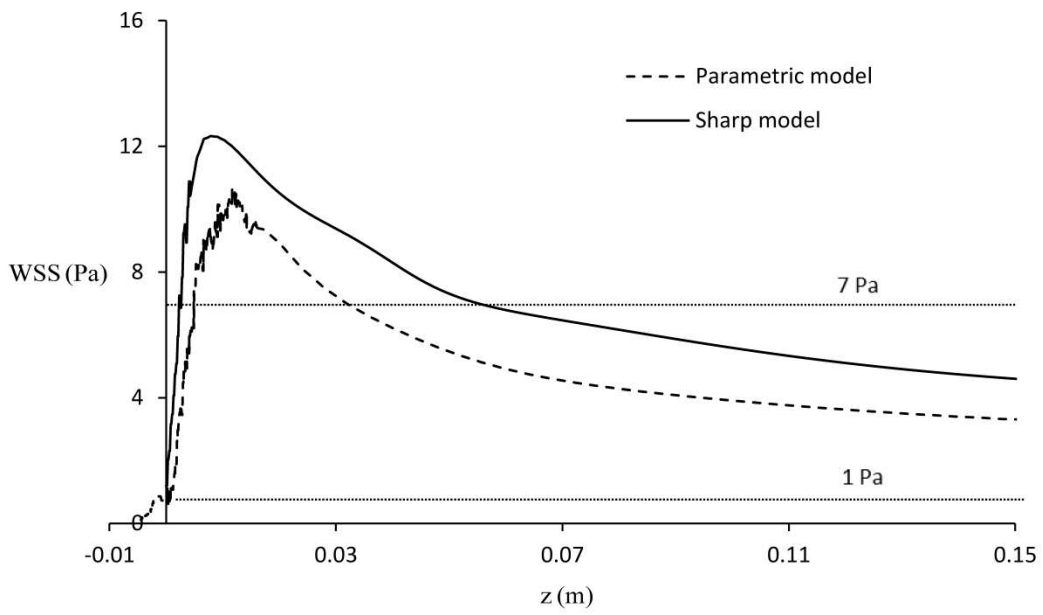ure 10 (a) shows that at $z=15\text{mm}$, the WSS distribution is more uniform with a low average value of 4 Pa in comparison with 5 Pa in a sharp junction. In Figure 10 (b), similar values of maximum WSS can be observed for both models (~14 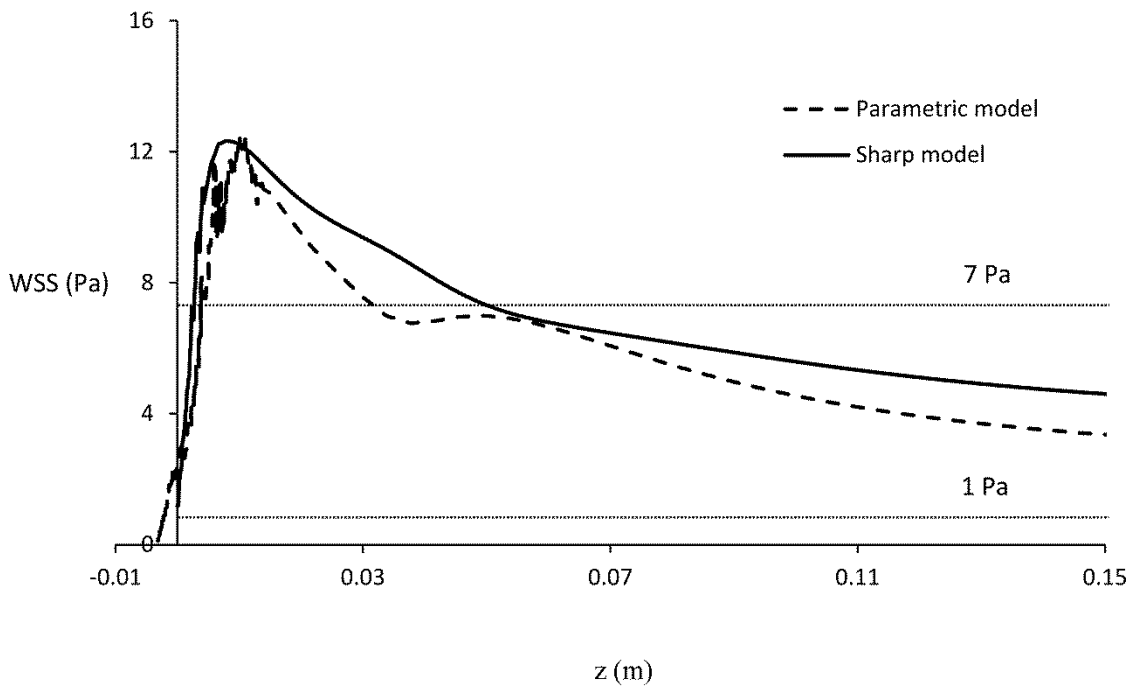Pa). In the smoothed model, the distribution of WSS is more intense at the beginning of the downstream flow, but a more uniform distribution of low values is

288   found at $z = 20\text{mm}$ in comparison with the sharp model. It is found in Figure 10 (c) that the

289   recirculation area has a similar but weak influence on the WSS distribution in a rounded junction

290   comparing those observed in a sharp junction for a confluence angle of $125°$ shown. In order to

291   quantify how much the recirculation affects the WSS for different branching angles, a two

292   dimensional plot of WSS on a surface centerline is presented in Figure 11.
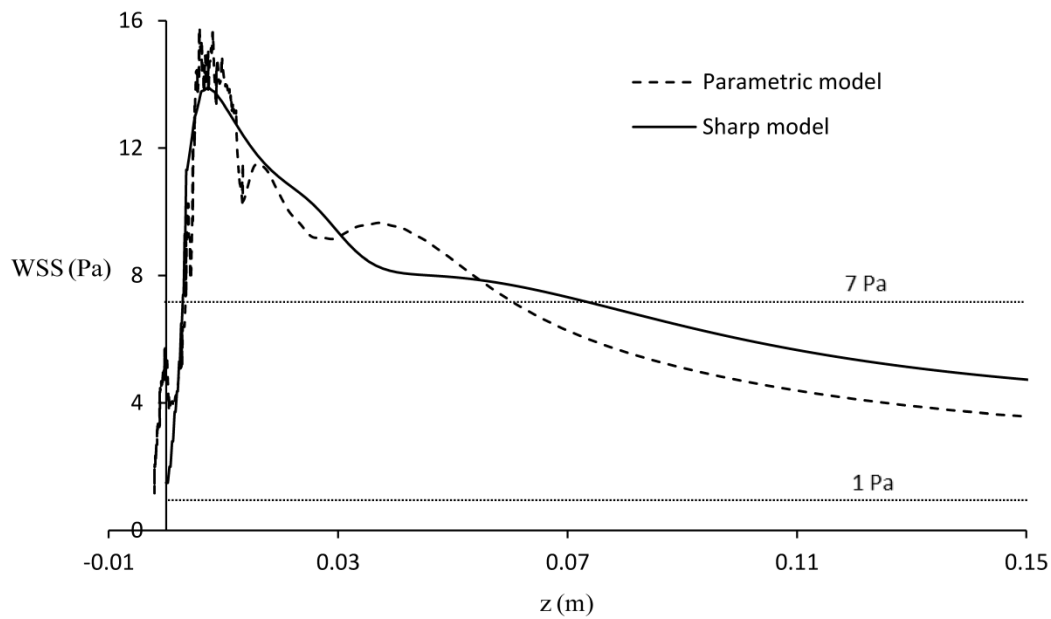
(a) 45°

293

(b) 85°

294

(c) 125°

295

Figure 11. WSS at the surface center line versus z of parametric model and sharp model, respectively
for branching angles (a) 45°, (b) 85° and (c) 125°.

The dashed lines and solid lines in Figure 11 show the WSS as a function of z for the smoothed and

sharp junctions respectively for different branching angles of (a) 45°, (b) 85° and (c) 125°. Here, a

'healthy window' is defined as the area along z-direction within which the WSS is in the range of 1 Pa

to 7 Pa. The healthy window is an important factor to assess a design of a junction. In the figure, an

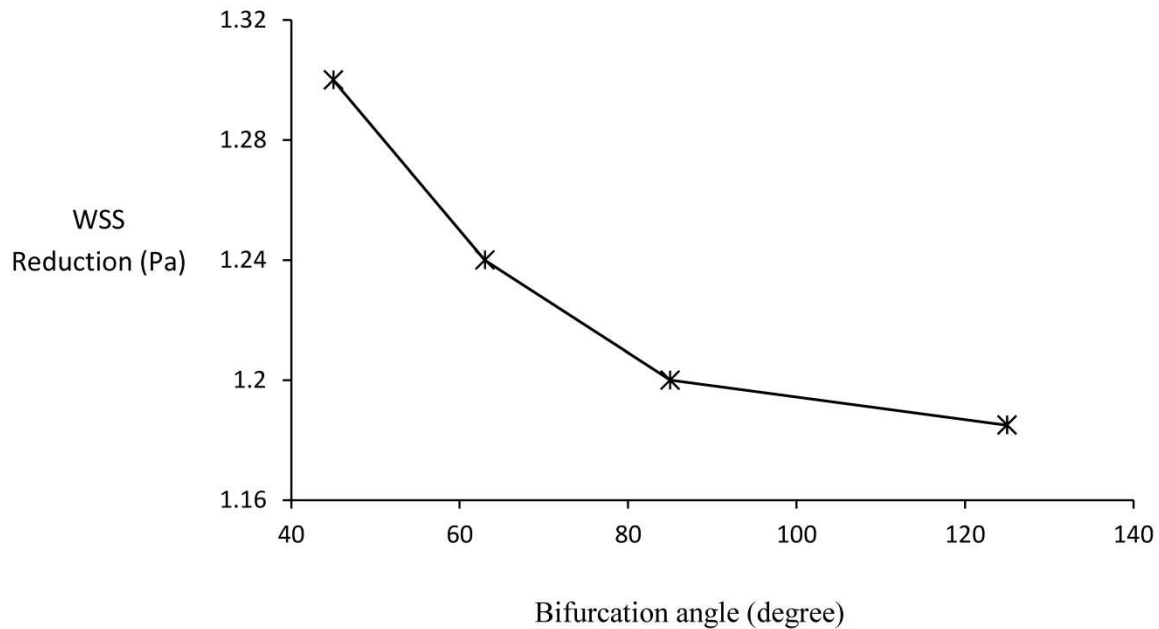area with healthy WSS is indicated using two dashed lines, representing 1 Pa and 7 Pa, respectively.

In Figure 11 (a), the maximum WSS of the smoothed junction is smaller than that of the sharp one.

The WSS values decrease for both junctions downstream. The healthy windows are $z \subset [0\text{m}, 0.005\text{m}]$

and $z \geq 0.06\text{m}$ for the sharp junction as seen in Figure 11(a). Those windows expanded to

$z \subset [0\text{m}, 0.01\text{m}]$ and $z \geq 0.035\text{m}$ for the smoothed junction from as seen in Figure 11(a). The smoothed

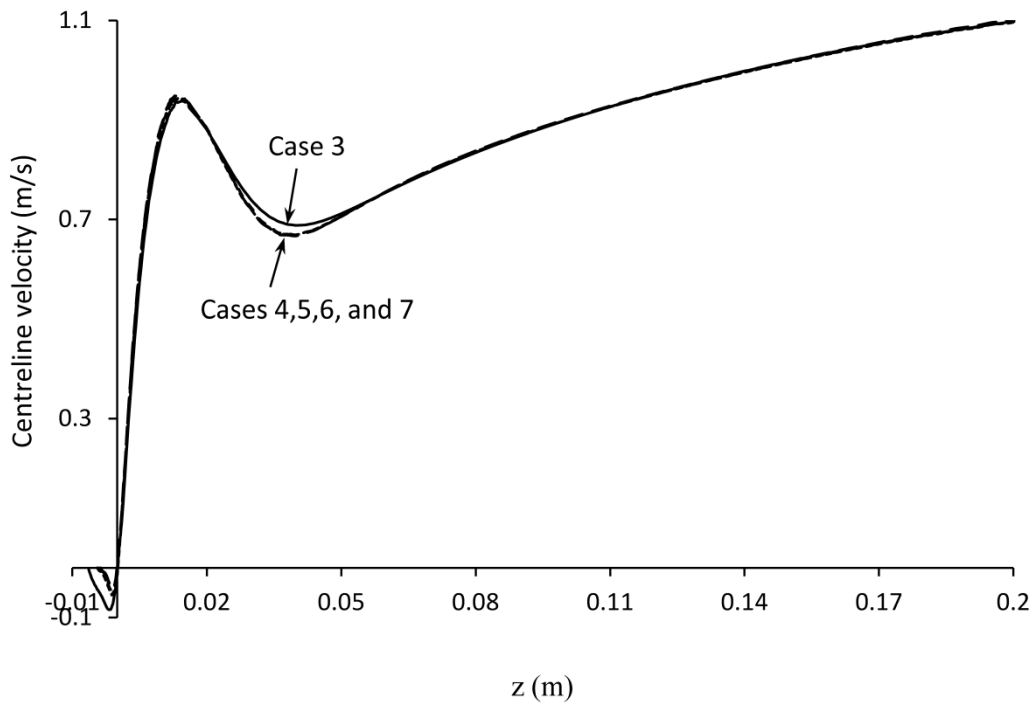design of the junction improves the WSS distribution with wider healthy windows. Healthy window

expansion can also be observed in Figures 11(b) and 11(c). All the smoothed junctions show a reduced

20

310   WSS and a more uniform WSS distribution at z=150mm downstream compared to the sharp junctions.

311   The reduced amount is however different for the three branching angles. A correlation between the

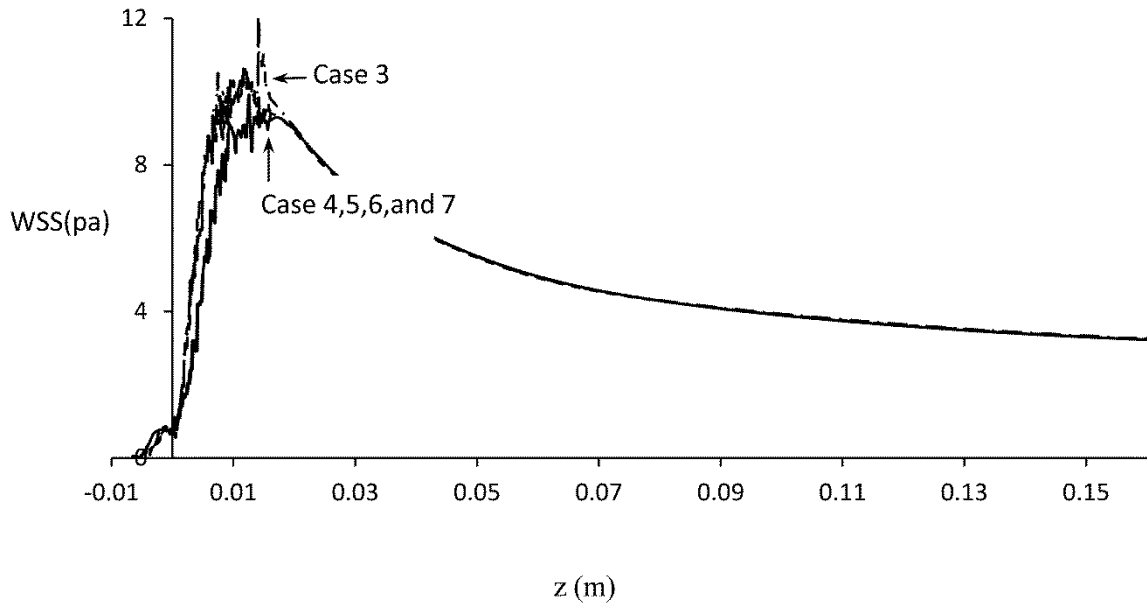312   WSS reduction and the bifurcation angle is shown in figure 12.

313

Figure 12. WSS reduction at z=0.15 (m) using parametric model compared with sharp bifurcations
versus bifurcation angles.

317   From Figure 12, it is seen that junctions with larger bifurcation angle results in a smaller WSS

318   reduction. Further increase the bifurcation angle, the WSS reduction decreases more slowly. This

319   indicates that the smoothed design has less effect on WSS reduction downstream for bifurcations with

320   larger angle.

321   In the parametric design model of a branch junction, $\overline{C}_{max}$ and its corresponding $\overline{V}$ are the most

322   important geometric parameters. A larger $\overline{C}_{max}$ leads to a smaller $\overline{V}$, thus a smaller branching area.

323   Further increasing $\overline{C}_{max}$, however, has a limited effect on the branching area as $\overline{V}$ will decrease more

324   slowly. In this section, CFD simulations are presented for smoothed junctions with different $\overline{C}_{max}$ for a

325   branching angle of $45°$ (cases 3 - 7). Figure 13(a) shows the central axial velocity as a function of z

326   while Figure 13(b) shows the WSS along the centerline as a function of z coordinate for those cases.
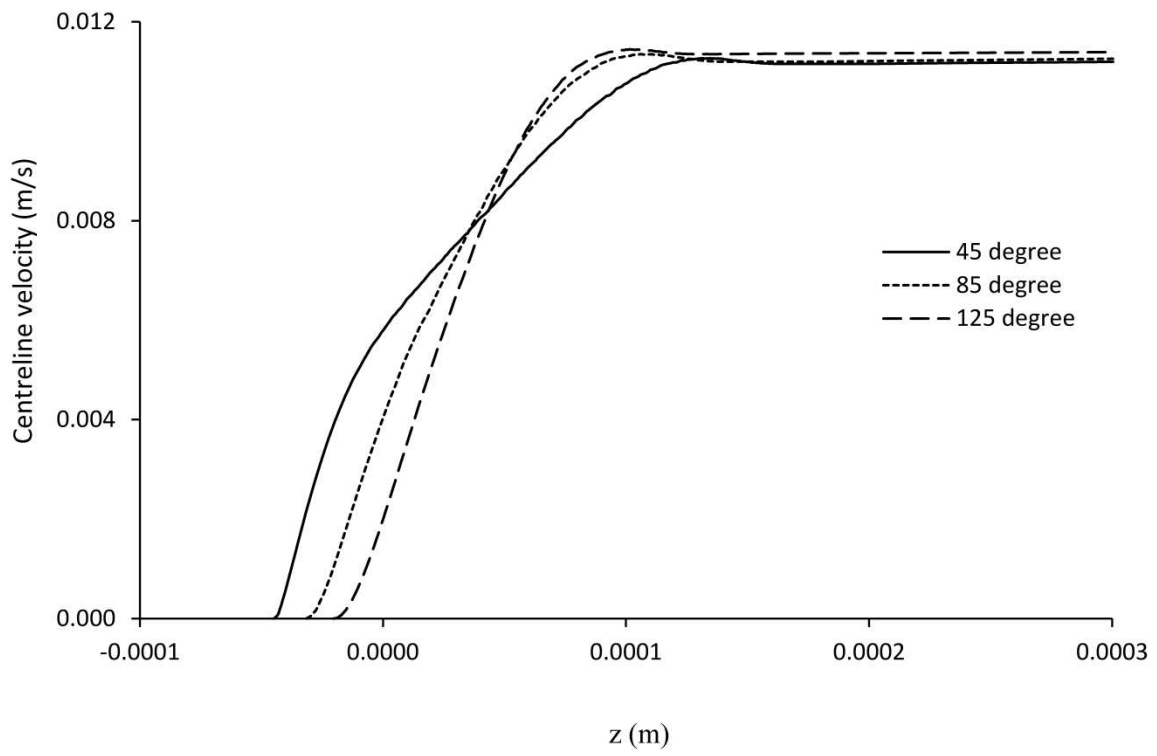
21

327

328

Figure 13. (a) Central axial velocities along center line for cases 3-7. (b) WSS at the surface center line versus z for cases 3-7.

In Figure 13(a), cases 4, 5, 6, and 7 show nearly identical velocity distributions. Only case 3 illustrates small deviations from the other cases in the area of z<0 and $z \in (0.02\text{m}, 0.05\text{m})$. Figure 13(b) indicates that WSS is different for the different junctions with different values of $\overline{C}_{max}$ in the area of z<0.02m.

335 Unsurprisingly case3 has the largest deviation. The WSS overlap with each other thereafter for all the

336 cases. It can be seen from table 2 that case 3 has the largest value of $\bar{V}$ and smallest value of $\bar{C}_{max}$

337 while cases 4 to 7 have different values of $\bar{C}_{max}$ but similar values of $\bar{V}$. This is why cases 4-7 have

338 similar central axial velocities and WSS. Although the velocities and WSS of case 3 show deviations

339 from the other cases, these deviations disappear downstream. These observations confirm that the

340 value of $\bar{C}_{max}$ and its corresponding $\bar{V}$ have effect on the distributions of central axial velocities and

341 WSS. The effects are, however, only in the local areas in contract to the influence from the branching
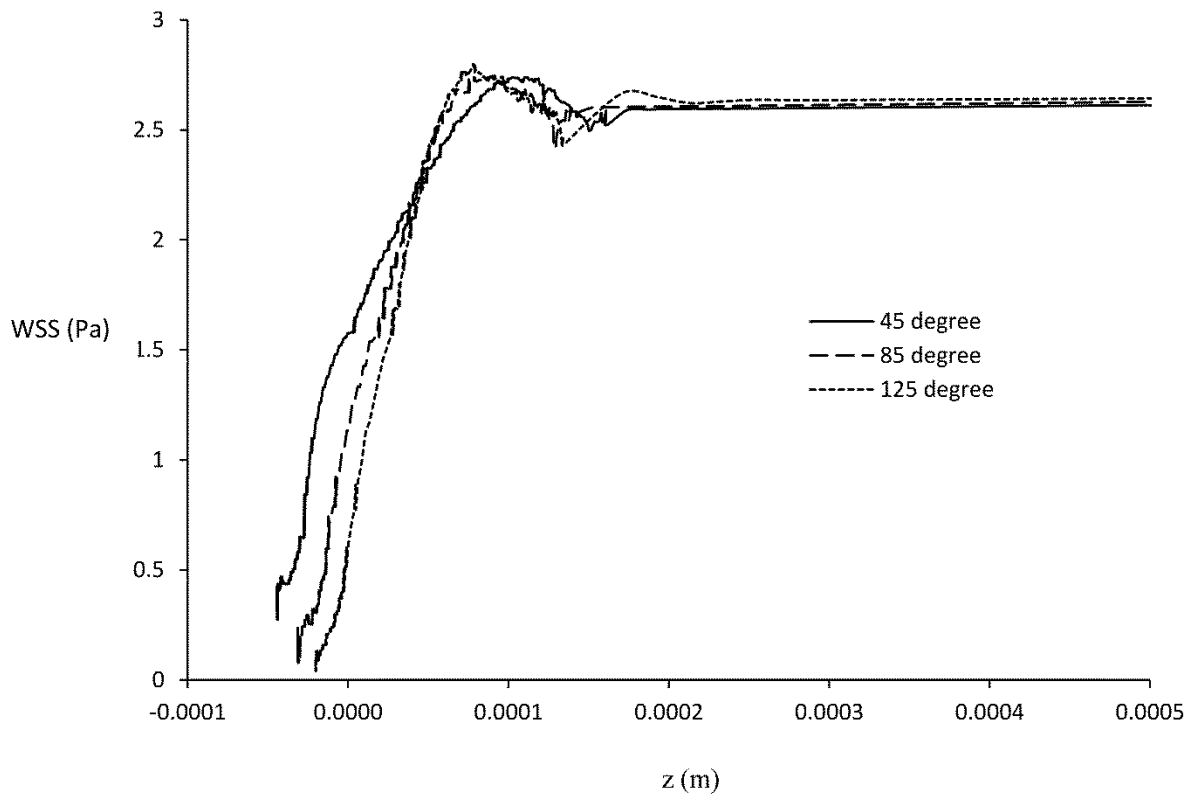
342 angle.

343 3.2. CFD analysis for micro-vascular vessels

344 Another important application of the parametric model is the design of micro-vascular networks for

345 supplying nutrients and oxygen in organ tissue engineering. In these micro-vascular networks, the

346 vessel diameters are in the range of tens of microns and the blood velocities are low which leads to a

347 small Reynolds number. In the simulations for the micro-vascular networks, all the diameters and inlet

348 velocities were scaled down by a factor of 0.01 from those in the previous section. The corresponding

349 Reynolds number is calculated as 0.06. Figure 14(a) compares the centerline velocities for cases with

350 branching angles of $45°$, $85°$ and $125°$ while Figure 14(b) shows the WSS at the surface centerline as

351 functions of z for the same cases.

(a)

352

(b)

353

Figure 14. (a) Centerline velocities for branching angles $45°$, $85°$ and $125°$ and (b) WSS at the surface center line versus z of parametric model branching angles $45°$, $85°$ and $125°$, using a low Reynolds number.

It can be observed from figure 14(a) that the centerline velocities fully develop immediately after its maximum value regardless of the branching angles. Surprisingly, in the area where z is negative, no negative velocity can be observed for all the cases which means that backflow and flow recirculation do not exist. It can also be observed from Figure 14(b) that the WSS are only different in a small area of z<0.0002 for all the cases of different branching angles.

4. Conclusions

In this paper, a set of CFD simulations were carried out to analyse the influence of the different geometric parameters in the branch design on flow behaviour. The geometric parameters include the branching angle, maximum curvature at the apex and volume of the branch. Firstly, a large Reynolds number of 600 was used in the simulations to represent arterial/venous flows. Then a small Reynolds number of 0.06 was applied to represent micro-vascular flows in a smaller lumen diameter. In the cases of large Reynolds number, it was found that in addition to manufacturing benefit, the smoothed junction has two advantages and one drawback. The advantages include: 1) it helps mixing the two flows better than the sharp junctions; and 2) they have large healthy windows of low WSS. The drawback is that the recirculation flow may occur in these smoothed junctions. The simulation results also revealed that different geometric parameters affect the flow behaviour differently: 1) a large branching angle tends to induce less recirculation flow and WSS reduction in smoothed junctions; and 2) the maximum curvature only affects the flow behaviour locally. For cases with low Reynolds number, the drawback does not exist because no recirculation was found in such cases. Therefore, designers are free to choose any $\overline{C}_{max}$ for desired branch angles without considering the effect of the smoothed apex.

383 **Conflict of interest statement**

384 We have no conflicts of interest to report.

385 **References**

386 Caro, C. G., 2008. Discovery of the role of wall shear in atherosclerosis. Arteriosclerosis, Thrombosis,
387 and Vascular Biology. 29**,** 158-161.

388 Cliff, W. J., 1976. Blood vessels. Cambridge: Cambridge University Press.

389 Coppola, G.; Caro, C. G., 2008. Arterial geometry, flow pattern, wall shear and mass transport:
390 potential physiological significance. Journal of The Royal Society Interface**.** 1-10 p. 2008.

391 Edelman, E. R., 1999. Vascular Tissue Engineering - Designer Arteries. Circulation Research. 85**,** 1115-
392 1117.

393 Friedman, M. H. et. al., 1983. Arterial geometry affects hemodynamics: a potential risk factor for
394 atherogenesis. Atherosclerosis. 46**,** 225–231.

395 Friedman, M. H.; Seed, W. A., 1993, Hemodynamic implications of a relation between coronary
396 geometry and pathology: Atherosclerosis. 98**,** 193–199.

397 Gibson, I.; Rosen, D. W.; Stucker, B., 2010. Additive manufacturing technologies: Rapid prototyping
398 to direct digital manufacturing. Springer 2010.

399 Han, X.; Bibb, R.; Harris, R., 2015. Design of bifurcation junctions in artificial vascular vessels
400 additively manufactured for skin tissue engineering. Journal of Visual Languages and Computing. 28,
401 238-249.

402 Hoch, E.; Tovar, G.; Borchers, K., 2014. Bioprinting of artificial blood vessels: current approaches
403 towards a demanding goal. European Journal of Cardio - Thoracic Surgery. 46**,** 767-778.

404 Kamel, R. A. et al., 2013. Tissue Engineering of Skin. Journal of the American College of Surgeons.
405 217**,** 533–555.

406 Kannan, R. Y. et al., 2005. The roles of tissue engineering and vascularisation in the development of
407 micro-vascular networks: a review. Biomaterials. 26**,** 1857-1875.

408 Kohler, U. et al., 2001. MRI measurement of wall shear stress vectors in bifurcation models and
409 comparison with CFD predictions. Journal of Magnetic resonance imaging. 14**,** 563-573.

410 Kolesky, D. et al., 2014, 3D Bioprinting of Vascularized, Heterogeneous Cell-Laden Tissue Constructs:
411 Adv.Mater. 26, 3124-3130.

412 Kucukgul, C. et al., 2013 3D hybrid bioprinting of macrovascular structures. Procedia Engineering. 59,
413 183-192.

414 Liu, G.; Wu, J.; Ghista, D. N. H., Wenhua Kelvin K.L. Wong., 2015. **H**emodynamic characterization of
415 transient blood flow in right coronary arteries with varying curvature and side-branch bifurcation
416 angles. Computers in Biology and Medicine. 64**,** 117-126.

417 Marshall, I. et al., 2004. MRI and CFD studies of pulsatile flow in healthy and stenosed carotid
418 bifurcation models. Journal of Biomechanics. 37**,** 679-687.

419 Miller, J. S., Kelly. et al., 2012. Rapid casting of patterned vascular networks for perfusable
420 engineered three-dimensional tissues. Nature Materials. 11.

421 Naito, Y. et al., 2011. Vascular tissue engineering: towards the next generation vascular grafts.
422 Advanced Drug Delivery Reviews. 65, 312-323.

423   Papaioannou, T. G.; Stefanadis, C., 2004. Vascular wall shear stress: basic principles and methods.
424   Hellenic Journal of Cardiology. 46**,** 9-15.

425   Patrick, JR, C. W., 2000. Adipose tissue engineering: The future of breast and soft tissue
426   reconstruction following tumor resection. Seminars in Surgical Oncology. 19: 302-311 p. 2000.

427   Rose, F., Oreffo, R., 2002. Bone Tissue Engineering: Hope vs Hype. Biochemical and Biophysical
428   Research Communications. 292**,** 1-7.

429   Rabinovitz, R. S. Levesque, M. J. Nerem, R. M. 1987. Effects of branching angle in the left main
430   coronary bifurcation: Circulation. 76: IV-387.

431   Ravensbergen, J. et al., 1995. Merging flows in an arterial confluence: the vertebra-basilar junction.
432   Journal of Fluid Mechnaics. 304: 119-141.

433   Ravensbergen, J. et al., 1997. The influence of the blunting of the apex on the flow in a Vertebro-
434   Basilar junction model. Journal of Biomechanical Engineering. 119**,** 195-205.

435   Wu, W.; Deconinck, A.; Lewis, J., 2011. Omnidirectional Printing of 3D Microvascular Networks: Adv.
436   Mater. 23**,** H178-H183.